Image Motion of Remote Sensing Camera With Wide Field of View Over the Antarctic and Arctic

Jinliang Han, Xiubin Yang, Wei Yue, Tingting Xu, Shaoen Wang, Lin Chang, and Chunlei Yang

***Abstract*—Imaging by the remote sensing camera with a wide field of view (WFV) is of great significance in the issue of polar environment. However, the instability of the image motion velocity poses a huge challenge to the observation task since the direction of the earth's rotation velocity keeps changing in the polar regions. The edge blur of polar image by the camera with the WFV is usually ignored. Therefore, a specific theoretical model that the camera images over the polar region is supposed to describe the instability distinctly. Mathematical expressions of the image motion velocity field are obtained with a novel method of velocity projection and coordinate transformation. The quantitative analysis of simulation reveals that the increasing anisotropy of the instantaneous image motion velocity field gets most significant near the poles. The value of modulation transfer function at the edge of the field of view decreased by 0.33%, which results in a discrepancy of sharpness in an image. The model is capable of explaining the edge blur, of the image from BNU-1, which provides a theoretical basis for the image motion compensation strategy of cameras with the WFV.**

***Index Terms*—Arctic and Antarctic, edge blur, image motion, optical remote sensing, velocity field model, wide field of view (WFV).**

I. INTRODUCTION

THE Arctic and the Antarctic are so crucial for ecological environment that many countries have never stopped researching and investigating the polar regions. In recent years, the global warming problem has been intensifying continuously due to humankind's activities against natural laws. The polar ecological environment urgently requires the attention of all mankind. However, the freezing weather in the polar regions is not appropriate for human activities, and it is extremely difficult to monitor the environment. Therefore, remote sensing has become a better method for polar scientific research [1]–[5].

Remote sensing of the topography and glaciers of the polar regions mainly applies the method of multiple image mosaic [6]–[9], which aids in seamless interpretation but reduces the airborne advantages of timeliness information by polar remote sensors. Optical remote sensors can obtain higher resolution images, but the captured scenes are limited by the field of view (FOV) [8]. Due to energy constraints, orbits of optical satellites are mostly sun-synchronous, and small FOV cameras cannot cover the poles easily. Therefore, imaging in the highest latitude area requires a long time period [1], which is not suitable for some specific observations [9]. Like the imaging of ice shelves, glaciers, and ocean currents, short time periods and high imaging quality are more important than high resolution due to the consistency of ground features. Cameras with a wide field of view (WFV) have the advantage of a large imaging coverage width [10]–[12], which improves the timeliness of imaging and reduces the task of image mosaicking. For polar remote sensing, WFV cameras with a width of millions can cover high-latitude regions easily and capture satisfactory images.

The image motion analysis of the optical remote sensing camera and the drift angle matching are important factors that affect the imaging quality [13], [14]. Time delay and integration (TDI) cameras [15] require accurate image motion velocity and the drift angle to compensate during imaging. The common method, used in small FOV and low latitude regions, calculates the velocity of image motion through the triangular proportional relationship. It calculates the drift angle of a certain point, such as the nadir point, to match the overall image plane [16], which cannot account for the edge effects of WFV. Wang *et al.* gave an image motion velocity vector calculation model through the coordinate transformation method [17], which is widely used in optical remote sensing due to its accuracy. Other methods under study include ray tracing method [18], [19] and optical flow method [20], [21]. The ray tracing method analyzes the point-to-point image motion at any position on the image plane and we draw on the idea.

With image motion analysis, image motion compensation (IMC) can make remote sensing images clearer [22], [23] through attitude control [16], [24], optics [25], and image processing methods [26]. The image motion for WFV is mostly analyzed over mid- and low-latitude regions [12], [27], while less attention is paid to the image motion of the camera with WFV over the poles, or its IMC strategy. Due to the particularity of the environment, the edge blur of the polar image is easy to be ignored. Therefore, the specific image motion model that the optical camera with WFV images over the polar region is studied to explain the edge blur.

The WFV model takes into account the nonlinearity of the optical path length due to the curvature of the earth and the

---

Manuscript received December 18, 2020; revised February 3, 2021; accepted March 12, 2021. Date of publication March 17, 2021; date of current version April 5, 2021. This work was supported in part by the National Natural Science Foundation of China under Grant 62005275 and in part by the Major Projects of the Ministry of Science and Technology under Grant 2016YFB0501202. *(Corresponding author: Xiubin Yang.)*

Jinliang Han, Wei Yue, Tingting Xu, and Shaoen Wang are with the Changchun Institute of Optics, Fine Mechanics and Physics, Chinese Academy of Sciences, Changchun 130033, China, and also with the University of Chinese Academy of Sciences, Beijing 100039, China (e-mail: 240358941@qq.com; 2710267013@qq.com; 1422168015@qq.com; wangshaoen19961112@163.com).

Xiubin Yang, Lin Chang, and Chunlei Yang are with the Changchun Institute of Optics, Fine Mechanics and Physics, Chinese Academy of Sciences, Changchun 130033, China (e-mail: yangxiubin@ciomp.ac.cn; fanglinchang@aliyun.com; rayontheon@foxmail.com).

Digital Object Identifier 10.1109/JSTARS.2021.3066626

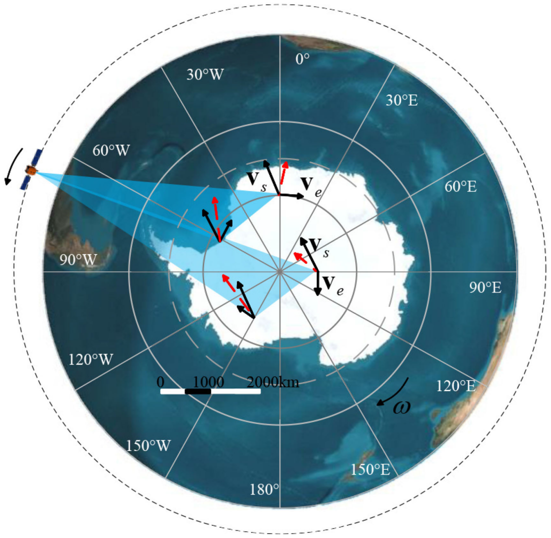

Fig. 1. Schematic diagram of the Antarctic remote sensing.

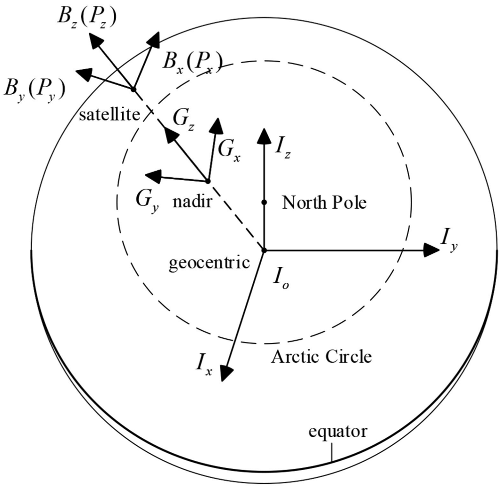

Fig. 2. Geography relation of optical remote sensor when imaging nadir.

anisotropy of image motion velocity at all latitudes and focuses on its mutation at high latitudes. This work would give a further improvement of the IMC strategy for polar satellites and contribute to the clear WFV imaging of polar optical satellites.

The remainder of this article is organized as follows. In Section II, the model of image motion is built on the basis of the sun's synchronous orbit with a qualitative analysis given to describe the fluctuation of the polar image by the camera with a WFV. Specific expressions are given while analyzing the image motion velocity field of the camera. In the meantime, the combination of the coordinate transformation and velocity projection is introduced to simplify the calculation. In Section III, under the condition that the camera images the polar region by push-broom, some essential parameters are simulated when the satellite moves to different positions. The instantaneous image motion velocity field and the change of drift angle are given, respectively, to show that there are significant differences between low-latitude areas and polar regions. In Section IV, an image quality degradation posed by the anisotropy of image motion is verified by an on-orbit image from BNU-1 of Beijing Normal University over the polar region.

II. MODEL OF IMAGE MOTION

A qualitative analysis of the ground objects velocity in the polar regions, where the latitude is approximately higher than 67°, is given first to illustrate the imaging characteristics of the polar regions clearly. Fig. 1 shows a schematic top view of the Antarctic. The area in blue indicates feasible imaging coverage of the satellite. The image motion velocity at one point is determined by the relative velocity $\mathbf{v}_s$ of the object to the satellite and the earth's rotation velocity $\mathbf{v}_e$ merely, while there is no attitude change of the satellite. The resultant velocities of the two variables are indicated by dotted vectors in red.

The anisotropy of image motion velocities in polar regions is intuitive in Fig. 1. From the resultant velocity shown at four imaging points, it can be argued that the velocity field presents a certain fluctuation around the pole. The reason is that the direction of the earth's rotation velocity in the polar regions are changing rapidly. The feature of anisotropy would be more prominent in a remote sensing image covering the poles. Or rather, rotative image motion velocities have a major impact on a single image if the coverage area is wide enough. In order to make the theory more concrete, it is necessary to ascertain the image motion velocity for each pixel on the image plane according to the characteristics of the WFV. A model in polar regions is built so as to give quantitative analysis in this section.

A. Coordinate Systems and Methods

Establishing the coordinate systems shown in Fig. 2 is necessary for the quantitative analysis, in which all of them adopt the right-hand system [17], [28]. The coordinate systems involved in mapping from the object to the image plane are defined as follows.

1) Geocentric Inertial Coordinate System $I(I_x, I_y, I_z)$*:* The origin I_o is at geocentric. I_x points to the intersection of the orbital plane and the equatorial plane, and I_z points to the north pole. I_y is perpendicular to I_x and I_z.

2) Spacecraft Orbit Coordinate System $B(B_x, B_y, B_z)$*:* The origin is the satellite's center of mass on the orbit. B_x points to the direction of the satellite's velocity, and B_z points to the zenith through geocentric I_o. B_y is perpendicular to B_x and B_z.

3) Geographic Coordinate System $G(G_x, G_y, G_z)$*:* The origin is at the nadir point on the Earth and the whole coordinate system is translated to the nadir point along B_z by the spacecraft orbit coordinate system, so that G_x is tangent to the trace circle of nadir on the ground.

The following simplifications are reasonable when building the model: regard the earth as a sphere; the geocentric point and centroid coincide; the geocentric latitude coincides with the geographic latitude; and the image plane coordinate system P, which will be distinguished during calculation, is related to the sensor, although it coincides with and the orbit coordinate system B temporarily.

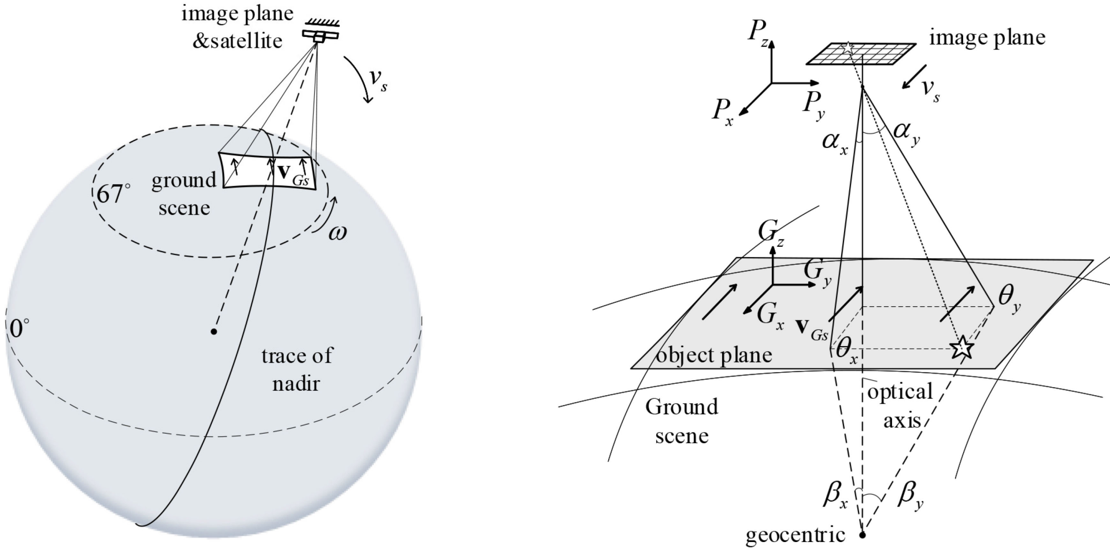

(a) (b)

Fig. 3. Schematic diagram of basic variables. (a) indicates the main velocities relationship when the satellite is over the pole. (b) is partial enlargement of the main area in (a) and gives the physical meaning in detail. The relationship between the basic variables, image plane, object plane, ground scene, and their coordinate systems are marked in (b).

We adopt an analytical approach to the image motion by combining the idea of ray tracing and the method of vector projection with coordinate transformation. Specifically, velocities involved are projected onto the object plan uniformly, which is convenient to calculate velocity field in the system G. The direction of the earth's rotation velocity in the polar region changes significantly as mentioned, and the value decreases rapidly while getting close to the pole. Therefore, the relative velocity and the rotation velocity are calculated in the spherical triangle on the earth directly for more accuracy. The image motion velocity field both on the object plane and the image plane can be obtained successively in combination with coordinate transformation.

B. Model of Instantaneous Velocity Field

In order to get a reliable model, the image motion caused by the satellite's movement and the earth's rotation are considered merely, which is universal in most imaging situations. The image motion velocity field of the camera with the WFV is calculated on the basis of the sun's synchronous orbit. The satellite imaging method is push-broom, and the optical axis of the camera is always pointed to the nadir point, which is the most common method in optical remote sensing.

When calculating the satellite's orbital velocity and its projection velocity on the ground first, some parameters in the calculation are defined as follows: The radius of the earth is R_e and the gravity constant is μ; H is the altitude of the satellite orbit and a is the length of semimajor axis. The direction of the satellite velocity $\mathbf{v}_s$ is tangent to the orbit, and its value can be obtained according to the law of universal gravitation or satellite's real velocity. The relative velocity to the nadir point $\mathbf{v}_{Gso}$ can be obtained by the projection of $\mathbf{v}_s$ in the geographic coordinate system G. The relationship is expressed by (1), where M_1 is the coordinate transformation matrix and e is the orbital eccentricity [28]

$$\mathbf{v}_{Gso} = M_1 \begin{bmatrix} -R_e(R_e+H)^{-1}v_s \\ 0 \\ 0 \end{bmatrix} \tag{1a}$$

$$M_1 = \begin{bmatrix} \cos\epsilon & 0 & -\sin\epsilon \\ 0 & 1 & 0 \\ \sin\epsilon & 0 & \cos\epsilon \end{bmatrix} \tag{1b}$$

$$\epsilon = \arccos \frac{a(1-e^2)^{-2}}{\sqrt{(R_e+H)(2a-R_e-H)}} \tag{1c}$$

where ϵ is the angle between the speed direction of the satellite and the x-axis of the instantaneous circular orbit coordinate system.

The relative velocity field of the ground in G, which corresponds to any point on the image plane, is $\mathbf{v}_{Gs}$. For more versatility and convenience in calculation, we employ the point's half FOV according to each pixel of the sensor. α_y is the optical axis deflection angle of a certain point in the vertical trace direction, β_y is the geocentric angle covered by the ground between the projection point and nadir, α_x is the point's deflection angle along the trace direction, and β_x is the corresponding geocentric angle. The latitudes are θ_y and θ_y. Fig. 3(a) shows the relative motion and position relationship among the earth, the satellite, and the image plane. Fig. 3(b) shows the relationship between the angles and latitudes above.

It is necessary to take into account the effect of the earth curvature when imaging by the camera with the WFV, even if the effect is minimal sometimes. The handling here is to treat the object plane, same as the XY coordinate plane in G, as a 2-D rectangle tangent to the earth at the nadir point so that it has a unified coordinate system for velocities. The relative velocity of the ground scene is transformed into the object plane in G through the method of coordinate transformation. Another advantage of this approach is that it does not need to account for the geometric distortion of the scene, but abstracts the observation task of the WFV into a more general observation situation. Therefore, $\mathbf{v}_{Gs}$ can be obtained from α_x and α_y at any point. The specific relationship is shown in (2), of which $\cos\beta_y$ in (2a) is the projection transformation. The relationship among β_x, β_y and α_x, α_y is determined by (3)

$$\mathbf{v}_{Gs} = M_2 \begin{bmatrix} \cos\beta_y & 0 & 0 \\ 0 & 1 & 0 \\ 0 & 0 & 1 \end{bmatrix} \mathbf{v}_{Gso} \tag{2a}$$

$$M_2 = \begin{bmatrix} \cos\beta_x & 0 & \sin\beta_x \\ 0 & 1 & 0 \\ -\sin\beta_x & 0 & \cos\beta_x \end{bmatrix} \begin{bmatrix} 1 & 0 & 0 \\ 0 & \cos\beta_y & \sin\beta_y \\ 0 & -\sin\beta_y & \cos\beta_y \end{bmatrix} \tag{2b}$$

$$\beta = \arcsin\left(\frac{R_e + H}{R_e}\sin\alpha\right) - \alpha \tag{3}$$

where M_2 is the conversion matrix from ground scene to object plane.

The same method is used when considering the earth rotation velocity in polar regions. In the geocentric inertial system I, $\mathbf{v}_e$ is the rotation velocity field of any point on the earth, ω is the rotation angular velocity of the earth, $\mathbf{R}_e$ is the radius of the earth, and θ is the geographic latitude of the point. $\mathbf{v}_{Ge}$ is the expression of rotation velocity field in G, and the relationship of $\mathbf{v}_e$ and $\mathbf{v}_{Ge}$ is

$$\mathbf{v}_e = \mathbf{R}_e \times \boldsymbol{\omega} \tag{4}$$

$$\mathbf{v}_{Ge} = M_2 \mathbf{v}_e. \tag{5}$$

The image motion of the nadir point is calculated first for accurate analysis. The calculation introduces the following variables: In the coordinate system G, the rotation velocity of the earth at the nadir is $\mathbf{v}_{Geo}$, and the angle between $\mathbf{v}_{Geo}$ and $\mathbf{v}_{Gso}$ is ρ_o. The corresponding geographic latitude is θ_o. Ω is the angle between the satellite and the ascending node. The specific position of the satellite in orbit can be determined by Ω. When the satellite runs for a circle, Ω changes from 0° to 360°. In the solar synchronous orbit, Ω can be calculated range of 68° to 112° and 248° to 292° over the Arctic and the Antarctic, where latitudes are higher than 67°N and 67°S. The equations of θ_o, ρ_o, and $\mathbf{v}_{Geo}$ are as (6) and (7), in which $-\mathrm{sgn}(\cos\Omega)$ is introduced to unify the process of up-going and down-going movement in one equation

$$\theta_o = \arcsin\left[\sin(\pi - i)\sin\Omega\right] \tag{6a}$$

$$\rho_o = \arccos\frac{\cos(\pi - i)}{\cos\theta_o} \tag{6b}$$

$$\mathbf{v}_{Geo} = \begin{bmatrix} -v_e\cos\rho_o \\ -\mathrm{sgn}(\cos\Omega)v_e\sin\rho_o \\ 0 \end{bmatrix} \tag{7}$$

where i is the orbital inclination.

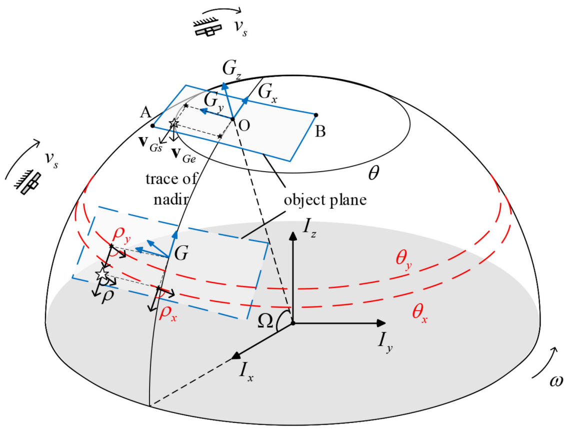

Fig. 4. Schematic diagram of intermediate variables. The essential intermediate variables are r and t, which can illustrate the details of the difference between high latitudes and low latitudes. The dotted line parts show not only the image plane at low latitudes, but also the operation of decomposing variables.

Accordingly, the earth rotation velocity field $\mathbf{v}_{Ge}$ in G can be expressed by the latitude of any point and the angle between the velocities. Furthermore, it can be expressed by the two corresponding angles α_x and α_y at any point as before.

Specifically, ρ is the velocity angle between $\mathbf{v}_{Gs}$ and $\mathbf{v}_{Ge}$, as shown in Fig. 4. ρ_x and ρ_y are the angles at the two points projected on the axes by any point marked as a star, and the geographic latitudes are θ_x and θ_y. The specific relationship is shown as follows:

$$\theta_y = \arcsin\left(\sin\theta_o\cos\beta_y + \sin\beta_y\cos i\right) \tag{8a}$$

$$\rho_y = \arccos\frac{\sin\theta_o - \cos\beta_y\sin\theta_y}{\sin\beta_y\cos\theta_y} \tag{8b}$$

$$\theta_x = \arcsin\left[\sin(\pi - i)\sin(\Omega + \beta_x)\right] \tag{9a}$$

$$\rho_x = \arccos\frac{\cos(\pi - i)}{\cos\theta_x}. \tag{9b}$$

For every point on the object plan, the latitude θ of the point can be ensured by taking (9a) into θ_o of (8a) and ρ is obtained successively by taking θ and θ_x into (8b), as follows:

$$\theta = \arcsin\left(\sin\theta_x\cos\beta_y + \sin\beta_y\cos i\right) \tag{10}$$

$$\rho = \arccos\frac{\sin\theta_x - \cos\beta_y\sin\theta}{\sin\beta_y\cos\theta}. \tag{11}$$

The resultant velocity field $\mathbf{v}_G$ of the ground scene at any point in the coordinate system G is shown as (12) when the orbit eccentricity e is assumed to be zero for a simplified model. There are only a few differences in (12) if e is nonzero according to (1):

$$\begin{aligned} \mathbf{v}_G &= \mathbf{v}_{Gs} + \mathbf{v}_{Ge} \\ &= M_2 \begin{bmatrix} -R_e(R_e + H)^{-1}v_s\cos\beta_y - v_e\cos\rho \\ -\mathrm{sgn}\left[\cos(\Omega + \beta_x)\right]v_e\sin\rho \\ 0 \end{bmatrix}. \end{aligned} \tag{12}$$

Finally, by transforming $\mathbf{v}_G$ into the coordinate system P, the image motion velocity field $\mathbf{v}_P$ can be obtained in the image

TABLE I
PARAMETERS OF NUMERICAL SIMULATION

Orbit Parameters	**Value**	**Optical Parameters**	**Value**
Inclination(i)	97.8°	Field of view(FOV)	53°
Eccentricity(e)	0	Pixel size	4.25μm
altitude(H)	739km	Focal length	42.7mm

plane. The relationship is shown as follows:

$$\mathbf{v}_P = M_0 \mathbf{v}_G \tag{13a}$$

$$M_0 = \begin{bmatrix} (-1)^n f/H & 0 & 0 \\ 0 & (-1)^n f/H & 0 \\ 0 & 0 & 0 \end{bmatrix} \tag{13b}$$

where M_0 is the conversion matrix from object plane to into the coordinate system P, n is the number of intermediate imaging times of the optical system according to the requirements, and f is the focal length.

III. SIMULATION

In this section, the imaging by a remote sensing camera with the WFV is simulated and analyzed. Quantitative description of the polar image motion is performed to verify the availability of the model. The simulation takes solar synchronous orbit as the foundation, under the conditions of no attitude change of the satellite. The camera is assumed to aim at the nadir point by push-broom imaging of the polar regions to compare with low-latitude regions. The parameters for simulation are listed in Table I.

A. Numerical Simulation

The value and direction of the image motion velocity field in the image plane are calculated according to the parameter list. Since the simulation based on the camera with the WFV at high latitudes, there is a great deal of variability for the rotation velocity, especially the direction, in the process of the satellite passing over the poles known from the qualitative analysis. Therefore, it is necessary to compare the distinct tendency of intermediate variables from velocities between low and high latitudes. Having been given the diagram in Fig. 4, the tendency curves of θ and ρ with Ω at different points are shown in Figs. 5 and 6 according to (10) and (11), respectively. The curves in the figure correspond to the nadir point O and the two endpoints A and B, on the diagonal of the object plane in Fig. 4, within the field of an instantaneous imaging by the camera.

Latitudes at different points still keep consistent tendency practically at low latitudes in Fig. 5, whereas the maximum latitudes of the three points present apparent discrepancy because of the WFV and the orbit inclination. As the difference between latitudes enlarges when the satellite runs over the poles, the respective trend of ρ is totally different as in Fig. 6. In the low latitudes, the maximum angle difference in the same plane is less than 20° both during the up-going and down-going, and the change is gentle, even if the FOV is wide. However, the angle in the image changes rapidly when entering the polar regions, and the angle difference is extremely unstable, which causes the anisotropy of image motion in the Arctic and the Antarctic.

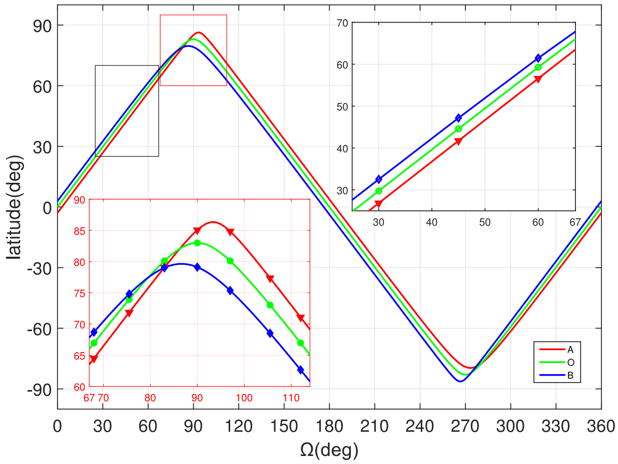

Fig. 5. Curves of the latitude (θ) in one period of the satellite orbit. The black rectangle marks a part of curves representing the changing trend of low latitude, while the red rectangle marks the polar latitude. The two subfigures correspond to the two marks, respectively.

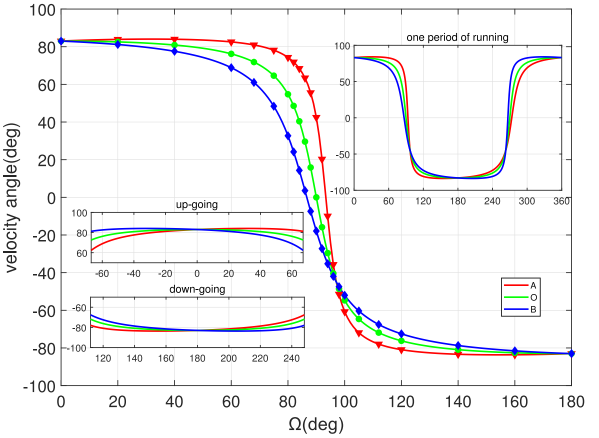

Fig. 6. Curves of the velocity angle (ρ). The main figure is a half-period change schematic focusing on the velocity angle in the polar range. The whole period curves, up-going curves over low latitudes, and down-going are shown in subfigures.

According to the image motion model, the velocity field produced by the earth rotation is demonstrated merely to draw the conclusions clearly. This is owing to the simulated image motion is caused by the movement of satellites and the earth rotation, and the former of which can usually be compensated conveniently during satellites running. The rotation velocity gradually decreases at higher latitudes, which is too small to merge compared to the satellite's velocity. Fig. 7 shows schematic diagrams of the rotation image motion velocity field, and Fig. 8 shows the corresponding drift angle when the satellite runs in different positions in orbit. The calculation formula of the instantaneous image motion velocity and the drift angle is

$$v_P = \sqrt{v_{Px}^2 + v_{Py}^2}$$

$$\phi = \arctan \frac{v_{Px}}{v_{Py}}.$$

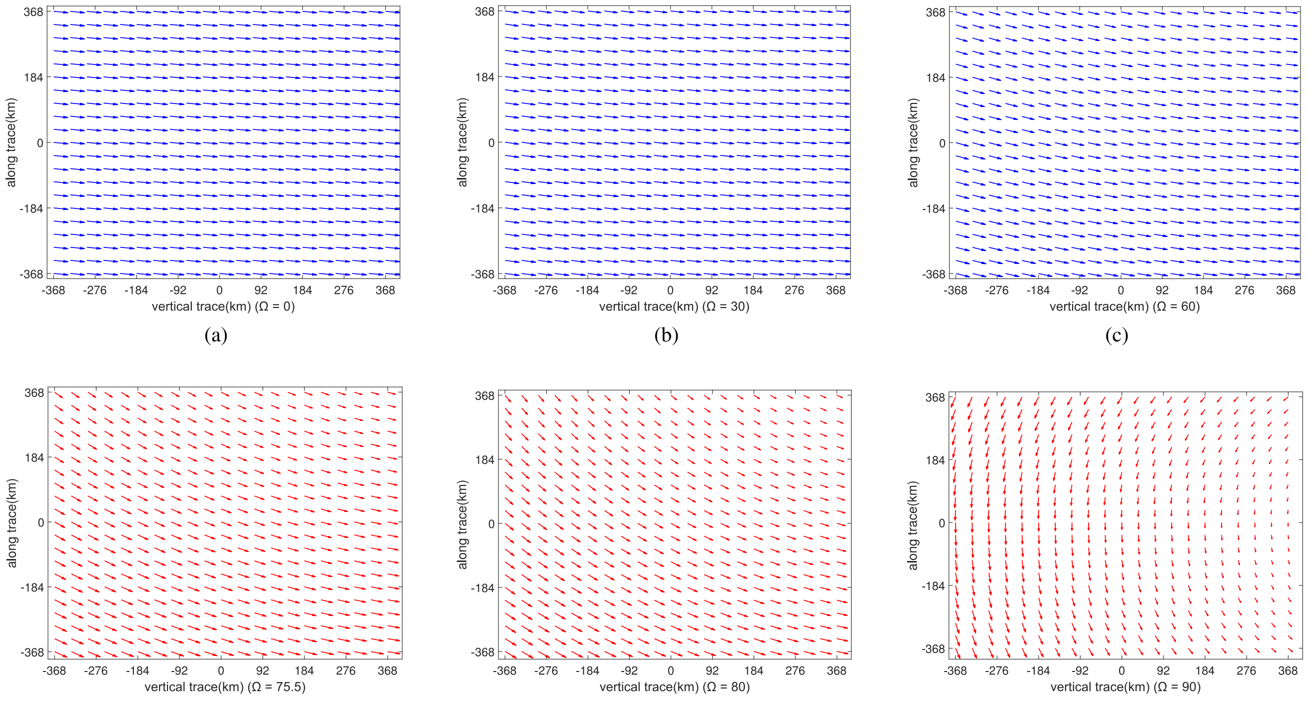

(a) (b) (c)

(d) (e) (f)

Fig. 7. (a)–(f) Schematic diagrams of the rotation image motion velocity field. The three blue subfigures are at low latitudes, and the red subfigures on the right represent high latitudes. The arrows point the rotation velocity vectors corresponding to some sampling points on the object plan and indicate the image motion on the image plan after satellite velocity compensated.

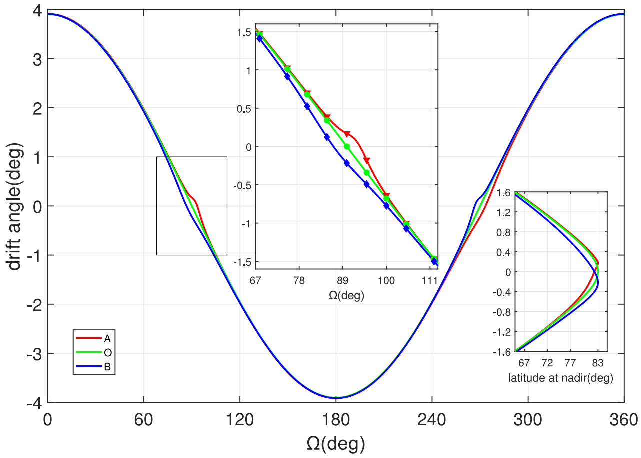

Fig. 8. Curves of the drift angle. The rectangle, corresponding to the middle subfigure, marks the drift angle of the Arctic WFV image. The subfigure on the right is the curve of drift angle changing with the latitude of the nadir point, which is more common in actual on-orbit applications.

In the first row of Fig. 7, though the image motion velocity field of $\Omega = 60^\circ$ starts to change slightly, the velocity field remains consistent overall in low latitudes. However, the motion velocity changes significantly in polar regions due to the wide imaging coverage. As the latitude gradually increases, the anisotropic image motion becomes more distinct too. When the camera rises to the highest latitude, where $\Omega = 90^\circ$, the difference in instantaneous image motion at each point is as much obvious.

As shown in Fig. 8, the drift angle of three pixels on the image plane, which are also distinguished with A, B, and O, varies with Ω during the satellite runs for one period on orbit. The tendency of drift angle is basically consistent, but a difference, which is most obvious near poles, occurs with latitude increasing. This difference expands from almost 0° to about 0.4°, and there is no symmetry during running. The subfigure on the right shows that when calculating the drift angle through the nadir latitude in actual situations, this enlarged difference still exists obviously. The calculated error will seriously affect the performance of IMC. Either of the figures shows the irregular characteristics of the drift angle in the polar region, especially near the pole.

B. Analysis of the Modulation Transfer Function

The modulation transfer function (MTF) can be used to indicate the degree of image quality degradation during imaging. The MTF could be divided into MTF_x generated by vertical image motion and MTF_y generated by horizontal image motion [15], [29], [30]. The specific relationship is as follows:

$$\text{MTF}_x = \text{MTF}_x \cdot \text{MTF}_r$$

$$\text{MTF}_s = \frac{\sin(\pi \cdot a \cdot f_N)}{\pi \cdot a \cdot f_N}$$

$$\text{MTF}_r = \frac{\sin\left[\pi/2 \cdot \Delta d/a\right]}{\pi/2 \cdot \Delta d/a}.$$

Among them, MTF_s is caused by uncompensable image motion, MTF_r is compensable image motion, and a is the pixel

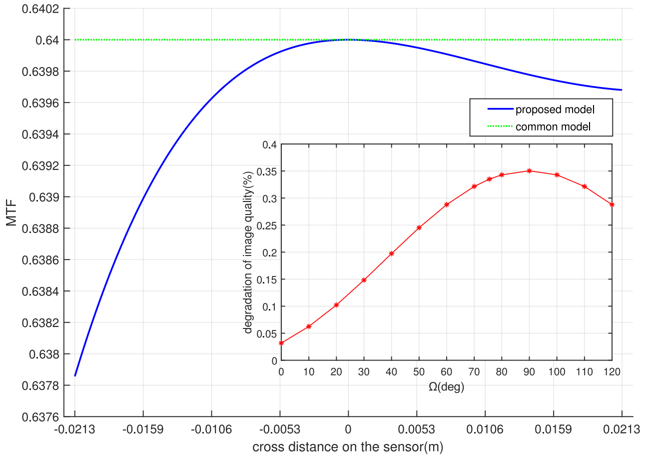

Fig. 9. MTF comparison in the vertical trace direction at the position of $\Omega = 75.5^\circ$. The blue curve is the image motion MTF of the line on the image plane where the nadir point is located. The right subfigure is the curve of the decrease ratio of MTF on the left of the image varying with Ω.

size. f_N is the Nyquist frequency, which can be expressed as $f_N = 1/2a$. Δd is the moving distance of a point on the image plane during the exposure time, which can be expressed as $\Delta d = v_P \cdot t_{\text{int}}$ and the camera exposure time t_{int} depends on the IMC strategy. MTF_y is similar to MTF_x; then, the synthesized MTF is as follows:

$$\begin{aligned}\text{MTF} &= \frac{\sin\left[\pi \cdot a \cdot 1/2a\right]}{\pi \cdot a \cdot 1/2a} \cdot \frac{\sin\left[\pi/2 \cdot \Delta d/a\right]}{\pi/2 \cdot \Delta d/a}\\ &= 0.64\frac{\sin\left[\pi/2 \cdot \Delta d/a\right]}{\pi/2 \cdot \Delta d/a}.\end{aligned}$$

The simulation graph of the MTF curve is shown in Fig. 9, when the satellite moves to the position of $\Omega = 75.5^\circ$, where the exposure time of the optical camera is 0.011 s and the integration level is 16 according to the general IMC strategy and signal-to-noise ratio of images. It is direct to evaluate the image quality of the TDI sensor using the MTF.

The common method [16] calculates image motion within tens of kilometers around the nadir point. The relationship between the object and the image plane is a proportional triangle, and the drift angle is calculated at a single point of the imaging center. When the FOV is expanded, the calculated image motion and the drift angle are still the same, which does not take into account the edge effects of the FOV. Its MTF is maintained in a straight line, as shown in the green dotted line in Fig. 9. The model in this article focuses on the difference in image motion and drift angle on the left, middle, and right sides of the same image plane at high latitudes. The calculated MTF has a significant difference in the vertical trace direction, as shown in the blue line in Fig. 9. The MTF of the image gradually decreases in the vertical direction from the middle to the sides and reaches the lower at the left edge of the image. The value of the MTF at the lowest decreased by 0.33% compared to the center. In other words, the closer it is to the edge of WFV, the greater the degradation of the image quality. The red curve in Fig. 9 shows the variation of the edge blur with Ω when the parameters are unchanged. When $\Omega = 0^\circ$, the degradation of image quality is only 0.03%. As the satellite up-going, the degradation gradually increases, reaching a maximum of 0.35% at the highest latitude. The decay rate gradually decreases because the earth's rotation velocity decreases in the polar regions.

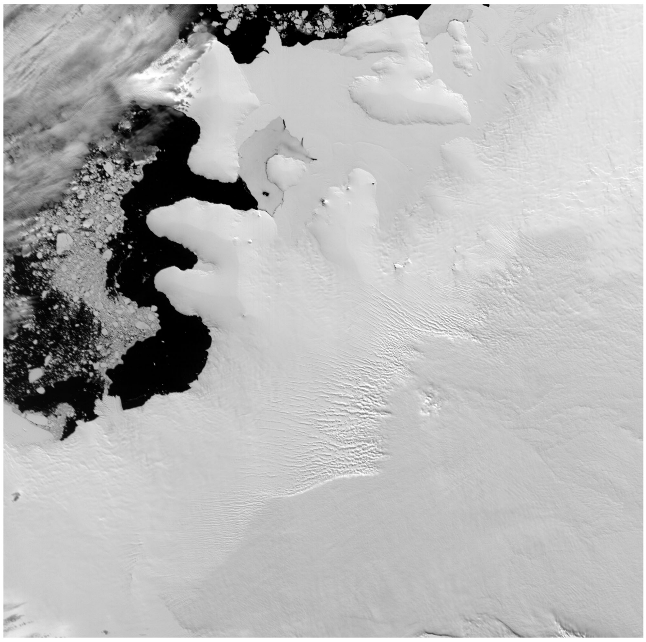

Fig. 10. Half-field image of a WFV remote sensing imaging by one of the two TDI-CMOS sensors. The geographic position of the nadir is 74°S, 79°W.

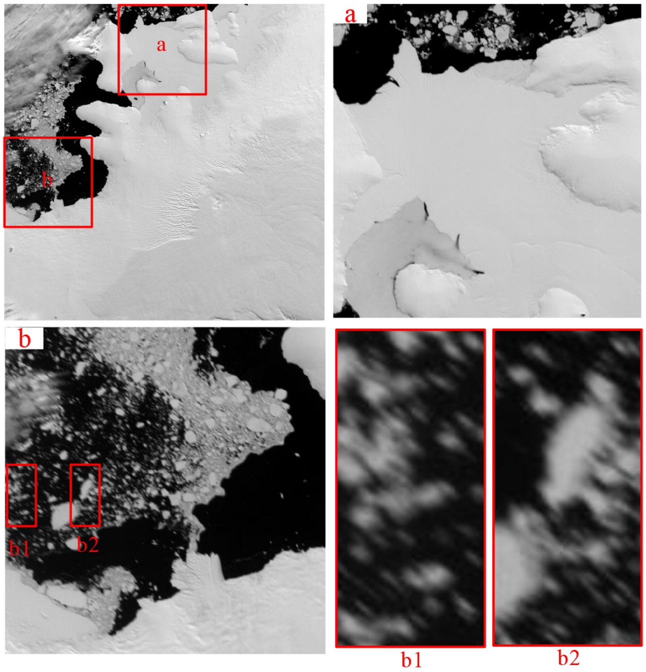

Fig. 11. Analysis of the image by zooming in. Subfigures are the different areas of the on-orbit image enlarged as a and b, and the two selected areas in b are enlarged as b1 and b2 to compare.

IV. ON-ORBIT VERIFICATION

In this section, the analysis results in Section III are verified through the experiment of the BNU-1 satellite. BNU-1 runs in

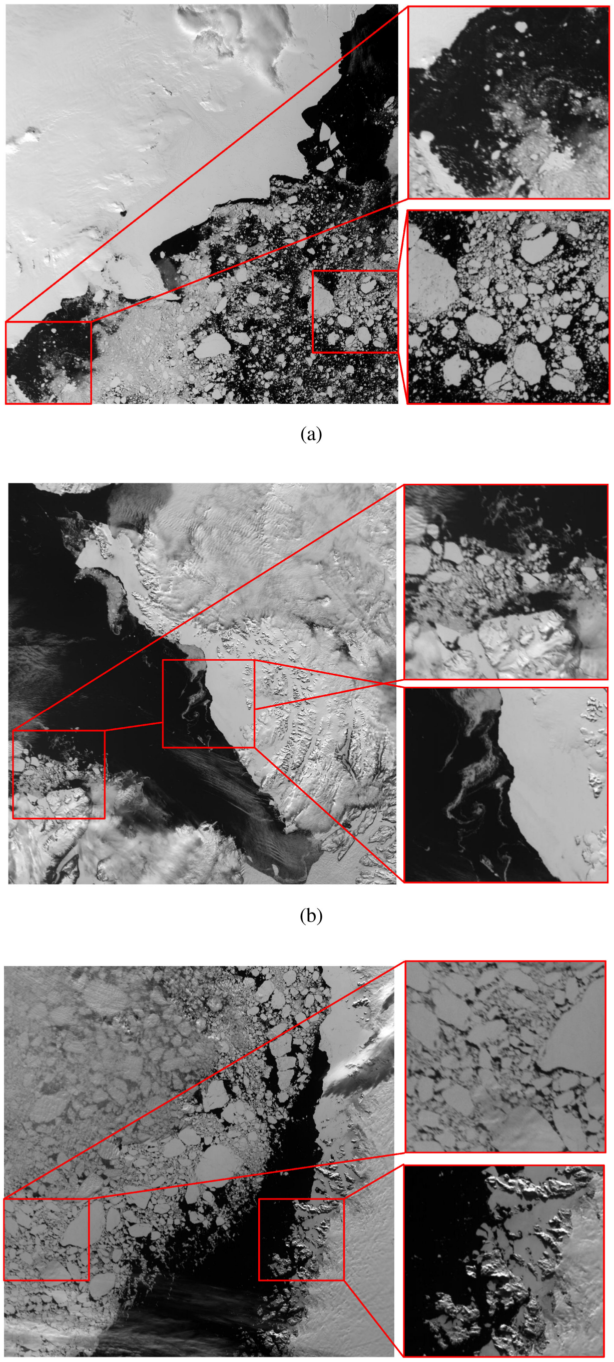

(a)

(b)

(c)

Fig. 12. Three half-field images of a WFV remote sensing imaging by one of the two TDI-CMOS sensors. (a) Position of the nadir is 75°S, 140°W. (b) Position of the nadir is 77°N, 77°W. (c) Position of the nadir is 74°N, 60°W.

sun-synchronous orbit with an altitude of 739 km. The satellite is equipped with a multispectral camera with a WFV. The camera is mainly used for polar climate and environmental monitoring, where latitude is 60–80°. The imaging width is 744 km, which corresponds to the FOV of 53°. The imaging sensor is time delay and integration CMOS (TDI-CMOS), and the pixel size is 4.25 μm. The ground sampling distance of the wide image is 73.6 m. A captured image of the camera above the Antarctica is shown in Fig. 9. Ω of the image is 255.5°, which corresponds to $\Omega = 75.5^\circ$ in Section III, thanks to the symmetry of the model, and the satellite has no attitude change during imaging, with the way of push-broom to the nadir.

The IMC method adopted on BNU-1 is mechanical compensation, which adjusts the entire image plane for drift angle of the nadir point. According to the analysis of on-orbit image data, the edge quality of WFV imaging has a significant decline.

Generated after the image motion compensated, the image is representative enough to illustrate the anisotropy of image motion with the WFV. The compensation strategy is the method of time-delay integration mapping, which eliminates the image blur at the nadir point. Corresponding to the nadir, the right side of the image gives the best sharpness in Fig. 10. On the contrary, the left side is gradually blurred as analyzed in MTF simulation. Specifically, Fig. 11 compares different local regions of the image by zooming in to illustrate the different degradation degrees of image quality intuitively. The definition of subfigure a is higher than b, which can be seen from the sharpness of the different ice floes in the two pictures, and the trailing corresponding to the earth rotation is more obvious in a. From the comparison of b1 and b2 and the serious degradation of image quality, it can be seen that the closer to the edge of the image, the greater the degree of image rotation blur. It is because that in the high latitude area, only small regional changes have very different image motion effects, which is simulated in Section III.

More polar WFV remote sensing images are shown in Fig. 12. Figures show the remote sensing image of periphery of Antarctica and Greenland. The most obvious position of edge blur is on the left side of the image. The subpictures on the right are the different areas of the WFV image by zooming in. The upper subpicture is a part with blurred edges, and the lower subpicture is a clearer comparison part.

V. CONCLUSION

In this article, for the remote sensing camera with the WFV, the particularity of push-broom imaging over the polar regions is proposed and verified. Combined with characteristics of high latitudes and the WFV, the model of imaging is given with simulation results. The following conclusions are drawn based on the results and the experiment.

1) Due to the characteristics of the earth rotation, the anisotropy of image motion on the polar region is more obvious, and the effect is more complicated than in low latitudes.
2) Although the image motion velocity field does not change much at low latitudes, it presents a drastic change for both the velocities angle and the direction of image motion at the high latitudes. There are obvious irregularities in the vicinity of the poles, where it is unreasonable for the model to be considered in accordance with low latitudes.
3) Fluctuating over the poles, the drift angles at different positions in an image plane with the WFV differ by up to 0.4°, and the calculation based on the nadir will result in an edge mismatch. In the MTF simulation of camera with the WFV, the edge quality of the image drops by

0.03% at zero latitudes but 0.35% at the highest latitudes, which is verified by the degradation of image from BNU-1 on orbit.

4) The universal IMC strategy is not suitable in high latitudes, and the calculation of the image motion and drift angle of polar satellites requires to be more exact and intelligent. It is foreseeable that the challenge of applying an effective IMC method to the polar image with the WFV must be faced.

The model explains the edge blur of polar images with the WFV, which may provide a theoretical basis for the polar remote sensing and IMC. It facilitates imaging missions in the Arctic and the Antarctic, which has not only the theory significance but also the practical significance. This article gives a model for the universal situation without swinging, which is a direction for future research.

REFERENCES

[1] J. Mouginot, E. Rignot, B. Scheuchl, and R. Millan, "Comprehensive annual ice sheet velocity mapping using Landsat-8, Sentinel-1, and RADARSAT-2 data," *Remote Sens.*, vol. 9, no. 4, Apr. 2017, Art. no. 364.

[2] R. Ressel, S. Singha, S. Lehner, A. Rosel, and G. Spreen, "Investigation into different polarimetric features for sea ice classification using X-band synthetic aperture radar," *IEEE J. Sel. Top. Appl. Earth Observ. Remote Sens.*, vol. 9, no. 7, pp. 3131–3143, Jul. 2016.

[3] T. Hollands, S. Linow, and W. Dierking, "Reliability measures for sea ice motion retrieval from synthetic aperture radar images," *IEEE J. Sel. Top. Appl. Earth Observ. Remote Sens.*, vol. 8, no. 1, pp. 67–75, Jan. 2015.

[4] M. Fahnestock, T. Scambos, T. Moon, A. Gardner, T. Haran, and M. Klinger, "Rapid large-area mapping of ice flow using Landsat 8," *Remote Sens. Environ.*, vol. 185, pp. 84–94, Nov. 2016.

[5] M. Dirscherl, A. J. Dietz, S. Dech, and C. Kuenzer, "Remote sensing of ice motion in Antarctica—A review," *Remote Sens. Environ.*, vol. 237, Feb. 2020, Art. no. 111595.

[6] R. Bindschadler *et al.*, "The landsat image mosaic of Antarctica," *Remote Sens. Environ.*, vol. 112, no. 12, pp. 4214–4226, Dec. 2008.

[7] H. Fengming *et al.*, "An improved landsat image mosaic of Antarctica," *Sci. China Earth Sci.*, vol. 56, no. 1, pp. 1–12, 2013.

[8] X. Li, R. Feng, X. Guan, H. Shen, and L. Zhang, "Remote sensing image mosaicking achievements and challenges," *IEEE Geosci. Remote Sens. Mag.*, vol. 7, no. 4, pp. 8–22, Dec. 2019.

[9] L. Chen, Y. Ma, P. Liu, J. Wei, and J. He, "A review of parallel computing for large-scale remote sensing image mosaicking," *Cluster Comput.*, vol. 18, no. 2, pp. 517–529, 2015.

[10] Z. Li, H. Shen, H. Li, G. Xia, P. Gamba, and L. Zhang, "Multi-feature combined cloud and cloud shadow detection in GaoFen-1 wide field of view imagery," *Remote Sens. Environ.*, vol. 191, pp. 342–358, Mar. 2017.

[11] L. Feng, J. Li, W. Gong, X. Zhao, X. Chen, and X. Pang, "Radiometric cross-calibration of Gaofen-1 WFV cameras using Landsat-8 OLI images: A solution for large view angle associated problems," *Remote Sens. Environ.*, vol. 174, pp. 56–68, Mar. 2016.

[12] C. Wang, Z. You, F. Xing, and G. Zhang, "Image motion velocity field for wide view remote sensing camera and detectors exposure integration control," *Acta Opt. Sinica*, vol. 33, no. 5, 2013, Art. no. 0511002.

[13] W. Zhong, H. Deng, Z. Sun, and X. Wu, "Computation model of image motion velocity for space optical remote cameras," in *Proc. IEEE Int. Conf. Mechatronics Autom.*, 2009, pp. 588–592.

[14] S. L. Smith, J. A. Mooney, T. A. Tantalo, and R. D. Fiete, "Understanding image quality losses due to smear in high-resolution remote sensing imaging systems," *Opt. Eng.*, vol. 38, no. 5, pp. 821–826, 1999.

[15] H. Wong, Y. Yao, and E. Schlig, "TDI charge-coupled-devices—Design and applications," *IBM J. Res. Develop.*, vol. 36, no. 1, pp. 83–106, Jan. 1992.

[16] W. Qiu and C. Xu, "Attitude maneuver planning of agile satellites for time delay integration imaging," *J. Guid. Control Dyn.*, vol. 43, no. 1, pp. 46–59, Jan. 2020.

[17] W. Jiaqi *et al.*, "Space optical remote sensor image motion velocity vector computational modeling, error budget and synthesis," *Chin. Opt. Lett.*, vol. 3, no. 7, pp. 414–417, 2005.

[18] T. Xu, X. Yang, S. Wang, J. Han, L. Chang, and W. Yue, "Imaging velocity fields analysis of space camera for dynamic circular scanning," *IEEE Access*, vol. 8, pp. 191574–191585, 2020.

[19] B. M. Miller and E. Y. Rubinovich, "Image motion compensation at charge-coupled device photographing in delay-integration mode," *Autom. Remote Control*, vol. 68, no. 3, pp. 564–571, 2007.

[20] J. Li and Z. Liu, "High-resolution dynamic inversion imaging with motion-aberrations-free using optical flow learning networks," *Sci. Rep.*, vol. 9, no. 1, pp. 1–12, Aug. 2019.

[21] C. Wang *et al.*, "Optical flow inversion for remote sensing image dense registration and sensor's attitude motion high-accurate measurement," *Math. Probl. Eng.*, vol. 2014, 2014, Art. no. 432613.

[22] S. K. Ghosh, "Image motion compensation through augmented collinearity equations," *Opt. Eng.*, vol. 24, no. 6, pp. 1014–1017, 1985.

[23] K. Janschek, V. Tchernykh, and S. Dyblenko, "Integrated camera motion compensation by real-time image motion tracking and image deconvolution," in *Proc. IEEE/ASME Int. Conf. Adv. Intell. Mechatronics*, 2005, pp. 1437–1444.

[24] X. Yang, X. L. He, K. Zhang Xu, and G. Jin, "Effect and simulation of the deviant angle error on TDI CCD cameras image," *Opto-Electron. Eng.*, vol. 035, no. 11, pp. 45–56, 2008.

[25] P. Jia, B. Zhang, and H. Sun, "Restoration of motion-blurred aerial image," *Guangxue Jingmi Gongcheng/Opt. Precis. Eng.*, vol. 14, pp. 697–703, 2006.

[26] S. Tao, X. Zhang, W. Xu, and H. Qu, "Realize the image motion self-registration based on TDI in digital domain," *IEEE Sens. J.*, vol. 19, no. 23, pp. 11666–11674, Dec. 2019.

[27] L. Yongchang, J. Longxu, L. Guoning, W. Yinan, and W. Wenhua, "Image motion velocity model and compensation strategy of wide-field remote sensing camera," *Geomatics Inf. Sci. Wuhan Univ.*, vol. 43, no. 8, pp. 1278–1286, 2018.

[28] H. Yan, J. Guang, C. Lin, and Y. Xiu-bin, "Image motion matching calculation and imaging validation of TDI CCD camera on elliptical orbit," *Guangxue Jingmi Gongcheng/Opt. Precis. Eng.*, vol. 22, no. 8, pp. 2274–2884, 2014.

[29] L. Xu, C. Yan, Z. Gu, M. Li, and C. Li, "Analysis of dynamic modulation transfer function for complex image motion," *Appl. Sci.-Basel*, vol. 9, no. 23, Dec. 2019, Art. no. 5142.

[30] X. B. Yang, G. Jin, L. Zhang, and Z. Y. Sun, "Satellite swaying to compensate earth speed research and imaging simulation analysis," *J. Astronaut.*, vol. 31, no. 3, pp. 912–917, 2010.

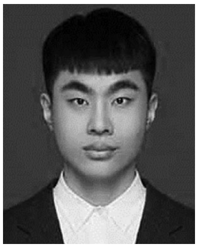

Jinliang Han received the B.Eng. degree in electronic information science and technology from Xiamen University, Xiamen, China, in 2018. He is currently working toward the M.S. degree in optical engineering with the Changchun Institute of Optics, Fine Mechanics and Physics, Chinese Academy of Sciences, Changchun, China.

His research interests include dynamic optical imaging and super-resolution imaging.

Xiubin Yang received the B.S. degree in physics from Nankai University, Tianjin, China, in 2006, and the Ph.D. degree in optical engineering from the Chinese Academy of Sciences, Changchun, China, in 2011.

He is currently a Professor with the Department of Space New Technique, Changchun Institute of Optics, Fine Mechanics and Physics, Chinese Academy of Sciences. His research interests include the dynamic imaging process of space optical camera, new mode of optical imaging, and advanced optical payload technology.

Wei Yue received the B.Eng. degree in measurement control technology and instruments from the Changchun University of Science and Technology, Changchun, China, in 2018. She is currently working toward the M.S. degree in optical engineering with the Changchun Institute of Optics, Fine Mechanics and Physics, Chinese Academy of Sciences, Changchun.

Her research interests include dynamic optical imaging and optical design.

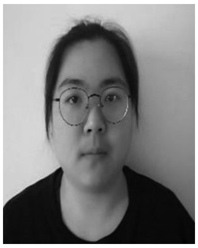

Tingting Xu received the B.Eng. degree in optoelectronics information science and engineering from Sichuan University, Chengdu, China, in 2017. She is currently working toward the Ph.D. degree in optical engineering with the Changchun Institute of Optics, Fine Mechanics and Physics, Chinese Academy of Sciences, Changchun, China.

Her research interests include optical design and dynamic optical remote sensing imaging.

Shaoen Wang received the B.S. degree from the Harbin Institute of Technology, Weihai, China, in 2019. He is currently working toward the M.S. degree with the Changchun Institute of Optics, Fine Mechanics and Physics, Chinese Academy of Sciences, Changchun, China.

His research interests include dynamic imaging and image processing.

Lin Chang received the B.S. degree in physics from Nankai University, Tianjin, China, in 2009, and the Ph.D. degree in optical engineering from the Chinese Academy of Sciences, Changchun, China, in 2014.

She is currently an Associate Professor with the Department of Space New Technique, Changchun Institute of Optics, Fine Mechanics and Physics, Chinese Academy of Sciences. Her research interests include satellite attitude control and the imaging of space optical cameras.

Chunlei Yang received the B.S. and Ph.D. degrees from the Beijing Institute of Technology, Beijing, China, in 2005 and 2010, respectively, both in aerospace science and technology.

He is currently a Professor with the Changchun Institute of Optics, Fine Mechanics and Physics, Chinese Academy of Sciences, Changchun, China. His research interests include the overall design and flight control technology of the aircraft.